ACS APPLIED POLYMER MATERIALS

pubs.acs.org/acsapm

Article

Fluorinated Glycidyl Triazolyl Polymers Exhibiting Thermally Stable Layered Structures and Sticky Hydrophobic Surfaces

Taichi Ikeda* and Masafumi Yoshio

Cite This: ACS Appl. Polym. Mater. 2026, 8, 3023−3032

Read Online

ACCESS | Metrics & More | Article Recommendations | Supporting Information

ABSTRACT: The side-chain fluorinated polymers bearing diethylene glycol monomethyl ether (EG2) and perfluorohexyl (C_6F_{13}) side groups were synthesized using glycidyl triazolyl polymers (GTPs). These GTPs were prepared via catalyst-free azide−alkyne cycloaddition between glycidyl azide polymers and electron-deficient alkyne derivatives. Postpolymerization functionalization enabled the successful production of fluorinated GTP homopolymers and copolymers with molecular weights on the order of 10^5 g mol^{-1}. Compared to previously reported side-chain fluorinated polymers, the fluorinated GTPs, denoted as GTP-EG2-*co*-C_6F_{13}*x* (where *x* indicates the C_6F_{13} content), display a range of distinctive and superior properties. Notably, they form well-organized layered structures with thermal stability up to 240 °C, significantly surpassing that of fluoropolymers with longer fluorocarbon chains such as C_8F_{17} and $C_{10}F_{21}$. This improved thermal stability is attributed not only to the high molecular weight but also to the longer and more flexible repeating units of the GTP backbone compared to vinyl-based polymers. The layered structures also serve as physical cross-links, contributing to higher storage modulus. The surface properties of the fluorinated GTPs were evaluated by contact angle measurements. Among them, GTP-EG2-*co*-C_6F_{13}25 exhibits particularly distinctive surface behavior. During the advancing contact angle measurement, the water droplet showed pronounced stick-and-slip motion, with a maximum contact angle exceeding the superhydrophobic threshold of 150°. In contrast, the receding contact angle was below 10°, satisfying the criterion for superhydrophilicity. Notably, this sticky hydrophobicity was achieved on the smooth surface (surface roughness <1 nm), offering promising advantages for practical applications requiring precise droplet positioning and strong droplet adhesion.

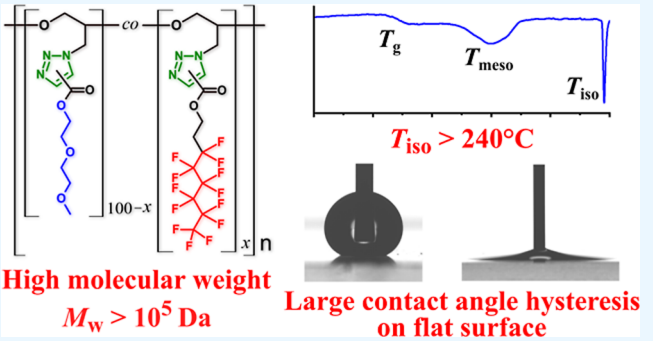

KEYWORDS: *fluorinated polymers, liquid-crystal polymers, postpolymerization functionalization, click chemistry, contact angle hysteresis, sticky hydrophobic surface*

INTRODUCTION

Side-chain fluorinated polymers are a class of polymers functionalized with fluorocarbon side groups.[1,2] Compared with commodity fluoropolymers such as polytetrafluoroethylene (PTFE) and polyvinylidene fluoride (PVDF),[3] they offer enhanced structural and functional tunability through variation in side-group composition.[4,5] Fluorocarbons possess a range of unique properties that are difficult to replicate with other chemical groups, including low surface energy,[6−8] distinctive ferroelectric behavior,[9,10] exceptional chemical and thermal stability,[11] and mesogenic characteristics that promote liquid crystal formation.[12,13] However, perfluoroalkyl substances (PFAS) have faced criticism and strict regulation because of their environmental impact,[14] particularly their bioaccumulative potential.[15,16] The tendency for bioaccumulation is strongly dependent on fluorocarbon chain length. Fluorocarbons with chain lengths equal to or shorter than the perfluorohexyl group (C_6F_{13}) have been reported to be less toxic and less biopersistent than longer fluorocarbon compounds.[17,18]

According to previous reports, the C_6F_{13} group lies at the threshold of structural organization: polymers functionalized with fluorocarbon chains longer than C_6F_{13} tend to form layered structures, whereas those with shorter chains typically yield amorphous materials.[19,20] For example, acrylic polymers bearing C_6F_{13} side groups directly attached to the main chain fail to form organized structures.[19,20] In contrast, introducing an *N*-methylsulfonamide spacer between the main chain and the C_6F_{13} group has been reported to promote structural organization.[21,22] In general, shorter fluorocarbon chains result

Received: December 1, 2025
Revised: February 11, 2026
Accepted: February 12, 2026
Published: February 16, 2026

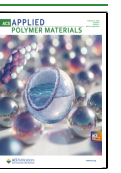

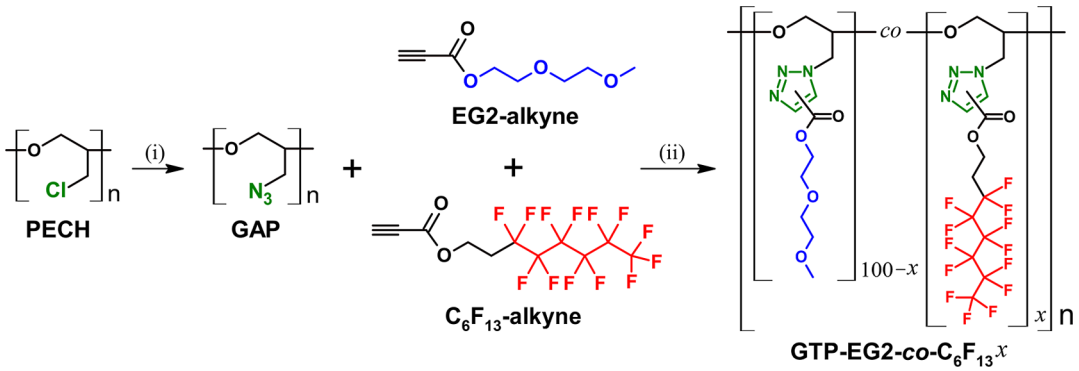

Figure 1. Synthetic scheme of GTP-EG2-*co*-$C_6F_{13}x$. PECH: Polyepichlorohydrin. GAP: Glycidyl azide polymer. GTP: Glycidyl triazolyl polymer. (i) NaN_3/DMF, 90 °C, 24 h. GAP was stored as a stock solution (solvent: DMF). (ii) 80 °C, 24 h.

in lower thermal stability of the organized structures due to weaker fluorocarbon−fluorocarbon interactions. A straightforward strategy to address this limitation is to increase the molecular weight of the polymer, which can enhance properties such as thermal stability and mechanical strength. However, synthesizing high-molecular-weight side-chain fluorinated polymers is challenging because conventional polymerization techniques often lead to premature precipitation caused by limited solubility, thereby hindering sufficient chain growth.[19−22] Although specialized methods such as surface-initiated polymerization can produce high-molecular-weight side-chain fluorinated polymers,[23] these techniques are not widely accessible and are unsuitable for large-scale production. Consequently, a postpolymerization functionalization strategy offers a practical and versatile alternative.[24,25]

In this study, we developed a novel class of side-chain fluorinated polymers using glycidyl triazolyl polymers (GTP). GTP serves as a representative platform synthesized by postpolymerization functionalization via azide−alkyne cycloaddition click chemistry.[26−30] Figure 1 illustrates the synthetic route of the copolymers with diethylene glycol methyl ether and C_6F_{13} side groups (GTP-EG2-*co*-$C_6F_{13}x$, where x denotes the C_6F_{13} content). Notably, complete side-chain functionalization was achieved even when glycidyl azide polymer (GAP) was reacted exclusively with C_6F_{13}−alkyne, enabling the synthesis of side-chain fluorinated homopolymer (GTP−C_6F_{13}) with molecular weight on the order of 10^5 g mol^{-1}. The fluorinated GTPs reported herein exhibit a range of distinctive and enhanced properties compared with previously reported side-chain fluorinated polymers. Some GTPs form well-organized layered structures with enhanced thermal stability up to 240 °C. These organized structures act as physical cross-links, contributing to higher storage modulus. During the advancing contact angle measurement on the GTP-EG2-*co*-C_6F_{13}25 film, the water droplet showed pronounced stick-and-slip motion, with a maximum contact angle exceeding the superhydrophobic threshold of 150°. In contrast, its receding contact angle was below 10°, satisfying the criterion for superhydrophilicity. Notably, this sticky hydrophobicity was achieved on the smooth surface (surface roughness <1 nm). These findings are discussed in the context of thermal, structural, rheological, and surface characterizations.

EXPERIMENTAL SECTION

Synthesis of C_6F_{13}−Alkyne

Tridecafluoro-1-*n*-octanol (18.2 g, 0.05 mol), cation exchange resin (1.6 g), and $MgSO_4$ (2.5 g) were mixed in toluene (25 mL). After bubbling nitrogen through the mixture for 10 min, distilled propiolic acid (6.2 mL, 0.10 mol) was added. The reaction mixture was heated at 100 °C under a nitrogen atmosphere for 24 h. After cooling to room temperature, the resulting solids were removed by filtration. The solids collected on the filter paper were washed with 150 mL of toluene during filtration. The filtrate was subsequently washed with aqueous NaOH (1.5 g/10 mL) and aqueous $NaHCO_3$ (1.5 g/10 mL) using a separation funnel. *Caution: Frequent venting of CO_2 is necessary to relieve pressure in the separation funnel caused by the reaction between propiolic acid and $NaHCO_3$. The cessation of CO_2 evolution indicates complete neutralization of propiolic acid.* The organic layer was collected, dried over $MgSO_4$, filtered, and concentrated using a rotary evaporator. The crude product was purified by column chromatography (SiO_2, hexane/ethyl acetate = 9:1). The colorless liquid product was obtained by distillation (2.3 Torr, 50−55 °C). Yield: 13.7 g (66%). ^{1}H NMR (400 MHz, $CDCl_3$): δ = 2.52 (m, 2H), 2.93 (s, 1H), 4.48 (t, J = 6.6 Hz, 2H); ^{13}C NMR (100 MHz, $CDCl_3$): δ = 30.5 (t, J = 22 Hz), 58.0, 74.1, 75.8, 108−122 (multiple small peaks for CF_2 and CF_3), 152.3.

Preparation of GAP Stock Solution

Polyepichlorohydrin (PECH) was cut into small pieces to facilitate dissolution in the solvent. PECH (4.0 g, 43 mmol) and sodium azide (NaN_3, 4.0 g, 62 mmol) were mixed in dry DMF (80 mL) in a 500 mL two-neck round-bottom flask. A condenser was attached to the center neck. The reaction mixture was heated at 90 °C with stirring under a stream of N_2 (100 mL min^{-1}) for 24 h in a fume hood. After cooling to room temperature, 320 mL of ethyl acetate was added with stirring, followed by the addition of 80 mL of distilled water. The mixture was transferred to a separation funnel, and the upper organic layer was collected, dried over $MgSO_4$, and filtered. Because a significant amount of DMF partitioned into the aqueous layer, 40 mL of dry DMF was added to the solution. The ethyl acetate was removed by evaporation at 35 °C while the pressure was gradually reduced to 1.6 kPa. The concentration by evaporation was stopped once DMF began to evaporate. The total mass of the solution was adjusted to 64 g by adding dry DMF. For this purpose, the weight of the empty flask must be measured before starting the experiment. It was determined that the 8.0 g solution contained 0.51 g of GAP (5.1 mmol repeating units).[30] This stock solution of GAP was stored at room temperature (approximately 20 °C) in the dark.

GTP−C_6F_{13} Homopolymer

After bubbling nitrogen through the GAP stock solution (8.0 g, 5.1 mmol repeating units) for 10 min, C_6F_{13}−alkyne (2.7 g, 6.5 mmol) was added. Since the addition of C_6F_{13}−alkyne induces precipitation of GAP, it was added dropwise over 1 min. The reaction mixture was stirred at 80 °C under a nitrogen atmosphere for 24 h. During the

https://doi.org/10.1021/acsapm.5c04519
ACS Appl. Polym. Mater. 2026, 8, 3023−3032

Table 1. Summary of GTP Synthesis

sample name	GAP[a] (g)	EG2-alkyne (g)	C_6F_{13}−alkyne (g)	ratio of alkynes[b]	ratio of alkyne/azide[c]	yield (%)
GTP−C_6F_{13}	0.51	–	2.7	0:1	1.3	96
GTP-EG2-*co*-C_6F_{13}75	0.51	0.28	2.1	1:3	1.3	97
GTP-EG2-*co*-C_6F_{13}60	0.51	0.45	1.6	2:3	1.3	98
GTP-EG2-*co*-C_6F_{13}50	0.51	0.56	1.4	1:1	1.3	97
GTP-EG2-*co*-C_6F_{13}25	0.51	0.84	0.68	3:1	1.3	96

[a]GAP was supplied as a stock solution. An 8.0 g stock solution contains 0.51 g GAP. [b]Molar ratio of EG2−alkyne/C_6F_{13}−alkyne. [c]Molar ratio of alkyne compounds and azide group in GAP.

reaction, the product became insoluble. The mixture was then diluted with dry DMF (50 mL) and stirred at 80 °C for 30 min, followed by decantation to remove the solvent. The resulting solid was washed again with DMF at 80 °C for 30 min, and the solvent was removed by decantation. The same washing procedure was repeated using different solvents, acetone (×2), dichloromethane (×2), and diethyl ether (×2) at 40 °C. The final product was dried under vacuum at 100 °C. Yield: 2.5 g (96%).

GTP-EG2-*co*-C_6F_{13}*x* Copolymer

The synthesis and workup procedure for the copolymer GTP-EG2-*co*-C_6F_{13}75 followed the same protocol as that used for the GTP-C_6F_{13} homopolymer. For GTP-EG2-*co*-C_6F_{13}60, dichloromethane was not used for washing the sample because the copolymer was slightly soluble in it. Since the other copolymers did not undergo phase separation during the reaction, the copolymer was recovered by precipitation in methanol. The resulting solid was washed with methanol (×2) and diethyl ether (×3), then dried under vacuum at 80 °C. The reaction conditions are summarized in Table 1.

GTP-EG2-*co*-C_6F_{13}75

Yield: 2.2 g (97%).

GTP-EG2-*co*-C_6F_{13}60

Yield: 2.1 g (98%). ^{1}H NMR (400 MHz, $CDCl_3$): δ = 2.61 (br, 1.2H), 3.20−4.00 (overlapping broad peaks, 6.6H), 4.30−4.85 (overlapping broad peaks, 4H), 8.12 (br, 0.08H), 8.30−8.90 (br, 0.92H); ^{13}C NMR (100 MHz, $CDCl_3$): δ = 30.5 (t, J = 21 Hz), 51.7, 57.1, 58.9, 64.3, 68.0−70.0 (br), 69.0, 70.5, 71.9, 77.0−78.5 (br), 106−122 (m), 129.6, 139.3, 139.8, 160.4, 160.8.

GTP-EG2-*co*-C_6F_{13}50

Yield: 1.9 g (97%). ^{1}H NMR (400 MHz, $CDCl_3$): δ = 2.61 (br, 1.0H), 3.20−4.00 (overlapping broad peaks, 7.5H), 4.30−4.85 (overlapping broad peaks, 4H), 8.12 (br, 0.08H), 8.30−8.90 (br, 0.92H); ^{13}C NMR (100 MHz, $CDCl_3$): δ = 30.4 (t, J = 21 Hz), 51.6, 57.1, 59.0, 64.3, 68.0−70.0 (br), 69.0, 70.5, 71.9, 77.0−78.5 (br), 106−122 (m), 129.7, 139.3, 139.7, 160.4, 160.8.

GTP-EG2-*co*-C_6F_{13}25

Yield: 1.6 g (96%). ^{1}H NMR (400 MHz, $CDCl_3$): δ = 2.64 (br, 0.5H), 3.20−4.00 (overlapping broad peaks, 9.8H), 4.30−4.85 (overlapping broad peaks, 4H), 8.13 (br, 0.09H), 8.30−8.90 (br, 0.91H); ^{13}C NMR (100 MHz, $CDCl_3$): δ = 30.4 (t, J = 21 Hz), 51.5, 57.1, 59.0, 64.3, 68.0−70.0 (br), 69.0, 70.5, 71.9, 77.0−78.5 (br), 106−122 (m), 129.7, 139.2, 139.7, 160.4, 160.8.

RESULTS AND DISCUSSION

Synthesis of GTPs

GAP was prepared by reacting PECH with NaN_3, purified by liquid−liquid extraction, and stored as a stock solution. Since GAP was not isolated in solid form, it can be handled safely despite being a high-energy, azide-rich compound with potential explosion hazards.[31] Nevertheless, the inherent risks associated with GAP should not be overlooked. Care must be taken to avoid contamination with metallic impurities during preparation, and the GAP solution should not be overly concentrated during evaporation.

Quantitative conversion of chlorine groups to azide groups was confirmed in our earlier works.[26,32] GTPs were synthesized via a catalyst-free azide−alkyne cycloaddition between GAP and an electron-deficient alkyne (Figure S2).[30] Reaction conditions are summarized in Table 1. All GTPs were obtained in excellent yields exceeding 95%.

The chemical structures of the GTPs were confirmed by IR and NMR spectroscopy. In the IR spectra, the absence of the azide absorption band at 2100 cm^{-1} indicated quantitative conversion of azide groups to triazole rings (Figure S1).[26] Although the GTP−C_6F_{13} homopolymer, GTP-EG2-*co*-C_6F_{13}75, and 60 copolymers underwent phase separation during the reaction, the azide−alkyne cycloaddition proceeded to completion. Because the phase-separated material appeared as a swollen gel, the alkyne compound was likely still able to diffuse into the gel and react with the remaining azide groups. All GTPs exhibited an intense characteristic peak at 1740 cm^{-1}, corresponding to ester C═O stretching. IR peaks corresponding to the glycidyl main chain, diethylene glycol, and fluorocarbon side chains overlapped in the fingerprint region. The peaks at 734, 811, 1011, 1080, and 1145 cm^{-1} (marked with stars in Figure S1) were assigned to C−F stretching vibrations, as their intensities increased with C_6F_{13} content. The characteristic peak at 3134 cm^{-1} was attributed to the ═CH stretching vibration of the 1,2,3-triazole ring.[33]

Figure 2 shows the ^{1}H NMR spectra of GTP copolymers. Since the GTP−C_6F_{13} homopolymer and GTP-EG2-*co*-C_6F_{13}75 copolymer were insoluble in common deuterated solvents, NMR characterization was not performed for these samples. The catalyst-free azide−alkyne cycloaddition yields structural isomers bearing 1,4- and 1,5-substituted triazole rings. The peaks labeled d and e in Figure 2a were assigned to the triazole protons of the 1,4- and 1,5-substituted products, respectively.[30,34] Based on the integrals of these peaks, the ratio of 1,4- to 1,5-substituted triazole units was approximately 9:1. In many examples of Cu-free GTP synthesis,[29,30,34] this isomer ratio was found to be independent of both the side-chain structures and the reaction conditions. The C_6F_{13} content in each copolymer was determined by comparing the integral of the overlapping peaks (c, f, and i) with that of peak j. The C_6F_{13} contents calculated from the ^{1}H NMR spectra were 61%, 51%, and 25% for GTP-EG2-*co*-C_6F_{13}60, 50, and 25, respectively. These values are in good agreement with the feed ratios of the corresponding alkyne derivatives used in the synthesis. ^{13}C NMR of GTPs are shown in Figures S3−S5.

Figure S6 shows the SEC traces of the GTPs used for molecular weight analysis. Based on the SEC data, the number-average molecular weight (M_n), weight-average molecular weight (M_w), and polydispersity index of GTP-EG2-*co*-C_6F_{13}25 were determined to be 3.3 × 10^5 g mol^{-1}, 5.5 × 10^5 g mol^{-1}, and 1.7, respectively (calibrated using polystyrene standards). These values are comparable to those previously

https://doi.org/10.1021/acsapm.5c04519
ACS Appl. Polym. Mater. 2026, 8, 3023−3032

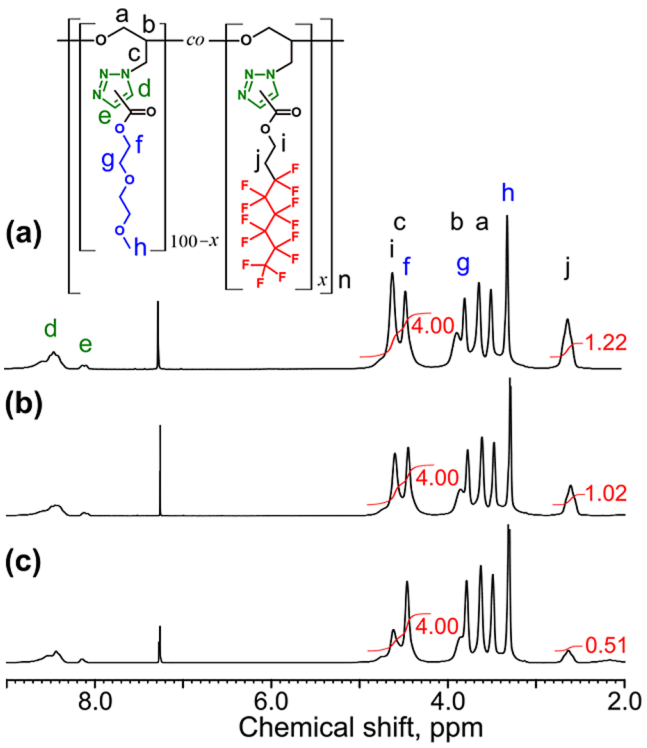

Figure 2. ^{1}H NMR spectra of GTP copolymers (400 MHz, $CDCl_3$). (a) GTP-EG2-*co*-C_6F_{13}60, (b) 50, and (c) 25 copolymers. The labeling scheme for peak assignment is shown at the top. Peak integrals (overlapping peaks c, f, i, and peak j) for determining copolymer composition are written in red.

reported for GTP derivatives.[30] No peak was observed for GTP-EG2-*co*-C_6F_{13}50. Several possible explanations may account for this result: (i) incomplete dissolution of GTP-EG2-*co*-C_6F_{13}50 in the solvent (DMF); (ii) adsorption of the polymer onto the column resin; or (iii) formation of self-assembled aggregates such as micelles due to its amphiphilic nature.[35] Since investigating the cause of this behavior falls outside the scope of this study, further characterization was not pursued. As all GTPs were synthesized from the same GAP stock solution, the M_n and M_w values of GTP−C_6F_{13} homopolymer were estimated to be 5.1 × 10^5 g mol^{-1} and 8.5 × 10^5 g mol^{-1}, respectively. Notably, these values are 1 order of magnitude higher than those reported for side-chain fluorinated polymers prepared via radical polymerization,[18,21,36] demonstrating the superiority of the postpolymerization functionalization approach.

Thermal Properties of GTPs

Thermal properties were characterized by differential scanning calorimetry (DSC), and the results are summarized in Figure 3a and Table 2. All DSC thermograms, except that of the GTP−C_6F_{13} homopolymer, exhibited a change in heat capacity at the glass transition temperature (T_g). Previous studies have reported that the T_g of fluorinated homopolymers is often difficult to detect.[21,25] Based on a comparison with the DSC thermogram of the GTP-EG2 homopolymer,[30] the observed T_g is attributed to the transition from the solid to the rubbery state, resulting from increased mobility of both the GTP main chain and the EG2 side chains. All DSC thermograms, except that of GTP-EG2-*co*-C_6F_{13}25, exhibited two endothermic peaks. Similar thermograms have been reported by other groups.[12,21,22,36,37] These two peaks are attributed to phase

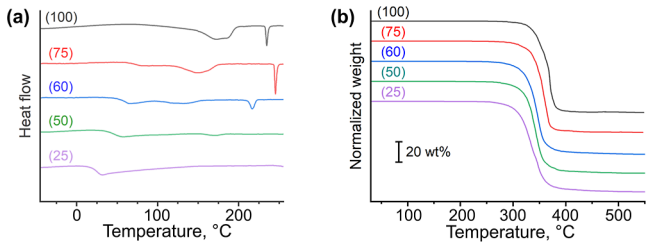

Figure 3. (a) DSC thermograms of GTPs. The number in parentheses indicates the C_6F_{13} content. Third heating cycle. Heating rate: 10 °C min^{-1}. (b) TGA traces of GTPs. Heating rate: 10 °C min^{-1}. N_2 atmosphere.

transitions from the solid or rubbery state to the smectic liquid-crystalline (LC) state (T_{meso}) and from the LC state to the isotropic state (T_{iso}). A cross-polarized optical microscopy image of GTP-EG2-*co*-C_6F_{13}75 at 175 °C shows an oily streak texture with distinct optical birefringence, indicating the formation of a layered LC phase (Figure 4a). Compared with results reported by other groups for C_6F_{13}- and even longer C_8F_{17}- and $C_{10}F_{21}$-side-chain fluorinated polymers, the T_{iso} value observed in this study is significantly higher (other groups: 60−210 °C; this study: >240 °C).[19−22,25,36,37] These differences are attributed to the substantially higher molecular weight of the GTPs compared with previously reported polymers. The enthalpy changes at T_{meso} and T_{iso}, denoted as ΔH_{meso} and ΔH_{iso}, respectively, were obtained from the DSC peak areas and are summarized in Table 2. These thermodynamic parameters are discussed in detail below, alongside the XRD results.

Figure 3b presents the thermogravimetric analysis (TGA) traces of the GTPs. The temperature corresponding to 5% weight loss is denoted as T_{d5}. The GTP−C_6F_{13} homopolymer exhibited no significant weight loss up to 300 °C (T_{d5} = 325 °C, Table 2). The T_{d5} values increased with C_6F_{13} content, suggesting that the fluorinated groups contribute to delaying the thermal degradation of the GTPs.

Organized Structure of GTPs

X-ray diffraction (XRD) measurements were conducted to investigate the organized structures of GTPs. Figure 4b shows the XRD profiles of GTP films measured at 38 °C after annealing at temperatures above T_{meso}. In the low-angle region of the GTP−C_6F_{13} homopolymer (Figure 4b, top), intense peaks corresponding to a layered structure were observed, including second-, third-, and fourth-order reflections. The layer spacing, calculated from the average of these four peaks, was 3.2 nm. The layered structure was also confirmed by AFM (Figure 4c). The layer spacing of 3.2 nm is comparable to that obtained by DFT calculations (Figure 4d). In the higher-angle region, small but distinct peaks corresponding to *d*-spacings of 5.0 Å and 4.7 Å were detected. The 5.0 Å spacing, frequently reported for side-chain fluorinated polymers, is attributed to the crystalline ordering of fluorocarbon chains.[19−21] In contrast, the 4.7 Å spacing was tentatively assigned to the packing of the 1,2,3-triazole rings, which has not previously been observed in GTPs because they were amorphous.[29,30] This ordering of the 1,2,3-triazole rings is considered to be induced by the packing of the C_6F_{13} groups.

GTP-EG2-*co*-C_6F_{13}75 and 60 copolymers also exhibited intense diffraction peaks corresponding to layered structures (Figure 4b). However, no pronounced peaks associated with crystalline ordering of the C_6F_{13} groups were observed. AFM

https://doi.org/10.1021/acsapm.5c04519
ACS Appl. Polym. Mater. 2026, 8, 3023−3032

Table 2. Thermal Properties of GTPs

sample name	T_g[a] (°C)	T_{meso}[b] (°C)	ΔH_{meso} (J g^{-1})	T_{iso}[c] (°C)	ΔH_{iso} (J g^{-1})	T_{d5}[d] (°C)
GTP−C_6F_{13}	–	174	12.8 ± 0.4	235	1.8 ± 0.0	325
GTP-EG2-*co*-C_6F_{13}75	61	151	8.2 ± 0.4	244	2.2 ± 0.1	315
GTP-EG2-*co*-C_6F_{13}60	50	132	3.1 ± 0.1	217	1.9 ± 0.0	300
GTP-EG2-*co*-C_6F_{13}50	33	107	0.2 ± 0.0	168	0.8 ± 0.0	301
GTP-EG2-*co*-C_6F_{13}25	17	–	–	–	–	291
GTP−EG2[e]	4	–	–	–	–	273

[a]Glass transition temperature (onset value from the third heating cycle in DSC). [b]Transition from the solid or rubber state to the liquid-crystalline state (peak-top value from the third heating cycle in DSC). [c]Transition from the liquid-crystalline state to the isotropic state (peak-top value from the third heating cycle in DSC). [d]Temperature corresponding to 5% weight loss in TGA analysis. [e]Data was taken from the ref 30.

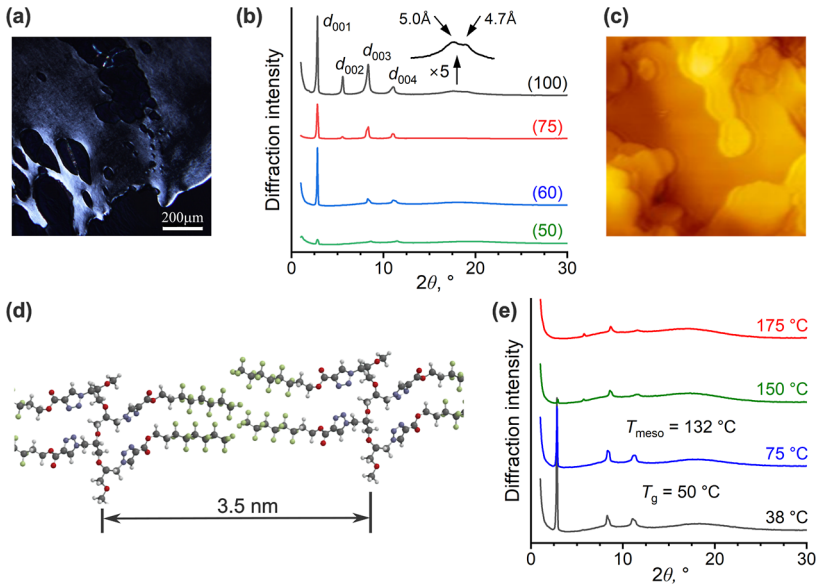

Figure 4. (a) Cross-polarized optical microscopy image of GTP-EG2-*co*-C_6F_{13}75 at 175 °C. (b) XRD profiles of GTP−C_6F_{13} homopolymer, GTP-EG2-*co*-C_6F_{13}75, 60, and 50 copolymers at 38 °C. The number in parentheses indicates the C_6F_{13} content. (c) AFM image of a GTP−C_6F_{13} film on glass. Scan area: 400 nm × 400 nm. (d) Proposed layered structure of GTP−C_6F_{13} homopolymer. The molecular structure was obtained by DFT calculations (B3LYP/6-31G*). (e) Temperature-dependent XRD profiles of GTP-EG2-*co*-C_6F_{13}60 during heating from 38 to 175 °C.

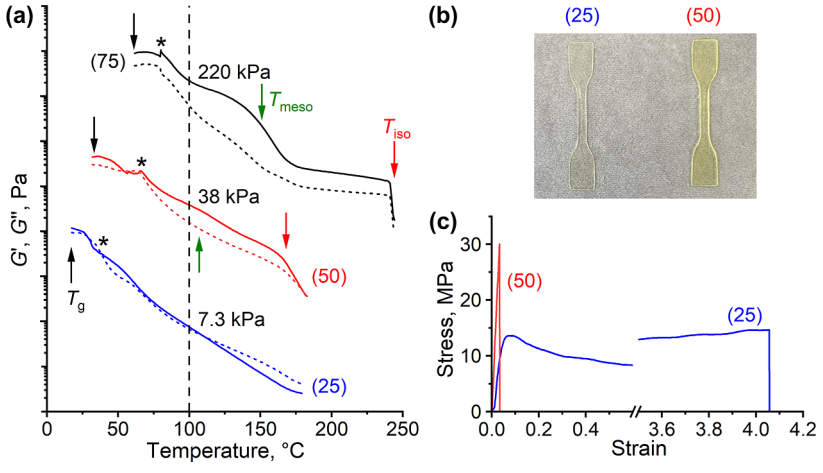

Figure 5. (a) Temperature-dependent viscoelastic properties of GTP-EG2-*co*-C_6F_{13}75, 50, and 25 copolymers. The number in parentheses indicates the C_6F_{13} content. For clarity, each data set is offset by 2 orders of magnitude. The storage (G') and loss moduli (G'') are shown as solid and dashed curves, respectively. T_g, T_{meso}, and T_{iso} are marked with black, green, and red arrows, respectively. Storage moduli at 100 °C are shown for comparison. (b) Dumbbell-shaped specimens of GTP copolymers used for tensile test. (c) Stress−strain curves of GTP-EG2-*co*-C_6F_{13}25, and 50 copolymers. Film thickness: 0.5 mm. Temperature: 16−17 °C.

measurements revealed that identifying the organized structures became increasingly difficult as the C_6F_{13} content decreased (Figure S8).

Figure 4e shows the temperature-dependent XRD profiles of the GTP-EG2-*co*-C_6F_{13}60 film during heating from 38 to 175 °C. Above the T_g, diffraction peaks corresponding to the

https://doi.org/10.1021/acsapm.5c04519
ACS Appl. Polym. Mater. 2026, 8, 3023−3032

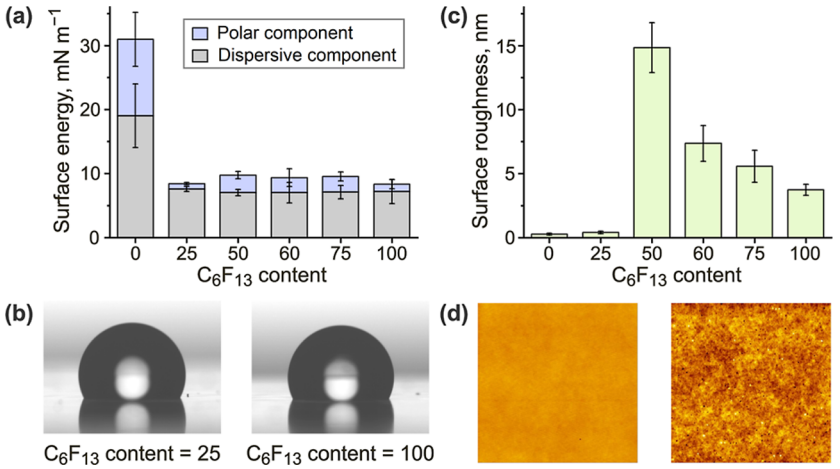

Figure 6. (a) Surface energies of GTP−C_6F_{13} and GTP−EG2 homopolymers and copolymers, determined from the contact angles of water, ethylene glycol, and diiodomethane droplets using the OWRK method. Values represent mean ± standard deviation (n = 5). (b) Photographs of water droplets on GTP-EG2-*co*-C_6F_{13}25 (left) and GTP−C_6F_{13} (right) films. Droplet volume: 2 μL. (c) Surface roughness of GTP films. Values represent mean ± standard deviation (n = 3). (d) AFM images of GTP-EG2-*co*-C_6F_{13}25 (left) and GTP−C_6F_{13} (right) films used to characterize surface roughness (scan area: 10 μm × 10 μm).

layered structure remained intense (75 °C in Figure 4e). This result demonstrates that, although the GTP backbone and EG2 side chains recover segmental mobility at T_g, the mobility of the C_6F_{13} groups remains limited, thereby preserving the well-defined layered structure. Although the absence of a pronounced peak associated with C_6F_{13} packing indicates low crystalline ordering of the C_6F_{13} groups, the ΔH_{meso} value suggests that the C_6F_{13} groups were phase-segregated from the EG2 side groups and interacted with each other within the domain. Above T_{meso}, the diffraction peaks weakened, indicating that the melting of the C_6F_{13} domains leads to a less-defined layered structure, and the copolymer transitions into a smectic liquid crystalline state (150 °C in Figure 4e). The ΔH_{meso} value decreased as the C_6F_{13} content decreased, due to the reduced amount of C_6F_{13} domains. In contrast, the ΔH_{iso} values were independent of the C_6F_{13} content in the cases of the GTP−C_6F_{13} homopolymer, GTP-EG2-*co*-C_6F_{13}75, and 60 copolymers. These results suggest that most of the polymer chains in those GTPs formed layered structures and that the ΔH_{iso} values originated from their order−disorder transitions. Similar temperature-dependent XRD profile changes were also observed for the other GTPs (Figure S7).

In the case of GTP-EG2-*co*-C_6F_{13}50, the peak intensity corresponding to the layered structure became weaker (Figure 4b), indicating a low degree of structural organization and suggesting that the majority of the copolymer had become amorphous. This result is consistent with the DSC data, which show small ΔH values at T_{meso} and T_{iso} (Table 2). AFM image of GTP-EG2-*co*-C_6F_{13}25 exhibited a completely flat surface, reflecting the amorphous nature of the polymer (Figure S8).

Mechanical Properties of GTPs

Since viscoelastic properties are sensitive to self-organized structures within polymeric materials, the GTPs were analyzed using a rheometer. Representative temperature-dependent profiles of the storage modulus (G') and loss modulus (G'') are shown in Figure 5a. Although the measurements were initiated above the T_g, behavior near T_g appeared unreliable due to slippage at the interface between the rheometer plate and the polymer sample. As the sample became tacky upon heating, reliable data could only be obtained at temperatures above those indicated by the asterisks in Figure 5a. For the GTP-EG2-*co*-C_6F_{13}75 copolymer (Figure 5a, top), the G' value decreased at T_{meso}, followed by a plateau region between 180 and 240 °C. G' exceeds G'' below T_{iso}, indicating that the organized structures function as physical cross-links and contribute to elastic properties in the GTPs. Upon transition from the smectic LC state to the isotropic state, both G' and G'' dropped sharply.

Similar temperature-dependent rheological property changes were observed for the GTP−C_6F_{13} homopolymer and the copolymers GTP-EG2-*co*-C_6F_{13}60 and 50 (Figures S10 and 5a). Notably, GTP-EG2-*co*-C_6F_{13}75 exhibited a broader temperature range for the smectic LC phase and a higher T_{iso} than the GTP−C_6F_{13} homopolymer. Generally, an increased C_6F_{13} content is expected to raise T_{iso} due to a stronger driving force for self-organization. However, complete functionalization with the C_6F_{13} side groups may induce excessive steric crowding and mechanical stress, which destabilize the organized structure. Incorporation of the EG2 side groups likely relieves this stress, thereby stabilizing the layered structures. Based on these considerations, one plausible explanation for the lower thermal stability of layered structures in vinyl-based fluorinated polymer is the shorter, less flexible repeating unit (−C−C−) relative to the GTP backbone (−C−C−O−), which increases mechanical stress. Thus, GTP is considered advantageous for realizing side-chain fluorinated polymers with enhanced thermal stability.

In the case of GTP-EG2-*co*-C_6F_{13}25 (Figure 5a, bottom), the values of G' and G'' decreased almost monotonically with increasing temperature. The G' value temporarily exceeded the G'' value at low temperatures, suggesting that the long chain length of GTP may enhance chain entanglement, which could act as transient physical cross-linking points.

From the G' values at 100 °C, it is evident that G' of the GTP copolymers increases significantly with C_6F_{13} content (Figure 5a). The markedly higher G' of GTP-EG2-*co*-C_6F_{13}75 compared with the other copolymers is likely attributable not only to its smaller temperature separation from T_g but also to its well-organized structure. The large G' drop around T_{meso} in GTP-EG2-*co*-C_6F_{13}75 also supports this idea.

https://doi.org/10.1021/acsapm.5c04519
ACS Appl. Polym. Mater. 2026, 8, 3023−3032

Table 3. Summary of Sessile-Drop Contact Angles, Surface Energies, and Surface Roughness

sample name	θ_{water} [a] (°)	θ_{EG} [b] (°)	θ_{DIM} [c] (°)	γ_d [d] (mN m^{-1})	γ_p [e] (mN m^{-1})	r_c [f]	R_a [g] (nm)
GTP−C_6F_{13}	116 ± 1	106 ± 2	99 ± 1	7.2 ± 1.9	1.2 ± 0.7	0.95	3.7 ± 0.4
GTP-EG2-*co*-C_6F_{13}75	110 ± 1	101 ± 3	99 ± 1	7.1 ± 1.0	2.4 ± 0.7	0.99	5.6 ± 1.3
GTP-EG2-*co*-C_6F_{13}60	108 ± 1	99 ± 1	98 ± 1	7.0 ± 1.6	2.3 ± 1.4	0.96	7.4 ± 1.4
GTP-EG2-*co*-C_6F_{13}50	109 ± 2	97 ± 3	99 ± 1	7.0 ± 0.5	2.7 ± 0.6	0.99	14.8 ± 1.9
GTP-EG2-*co*-C_6F_{13}25	117 ± 1	102 ± 1	100 ± 1	7.6 ± 0.4	0.8 ± 0.2	0.99	0.4 ± 0.1
GTP−EG2	76 ± 1	54 ± 1	44 ± 4	19.0 ± 5.0	11.9 ± 4.2	0.98	0.3 ± 0.1

[a]Static contact angle of a water droplet (2 μL). [b]Static contact angle of an ethylene glycol droplet (2 μL). [c]Static contact angle of a diiodomethane droplet (2 μL). Values are presented as mean ± standard deviation (n = 5). [d]Dispersive component of the surface energy. [e]Polar component of the surface energy. Measurements were conducted at 20 °C and 15−20% relative humidity. [f]Correlation coefficient of the OWRK method fitting. [g]Arithmetic mean roughness (area: 10 μm × 10 μm). Values are presented as mean ± standard deviation (n = 3).

Figure 5b shows dumbbell-shaped specimens of GTP-EG2-*co*-C_6F_{13}25 and 50 copolymers. GTP copolymers with C_6F_{13} content higher than 50% were too brittle to fabricate into dumbbell-shaped specimens. Figure 5c shows the stress−strain profiles of dumbbell-shaped specimens of GTP copolymers. Because the T_g of GTP-EG2-*co*-C_6F_{13}25 is close to room temperature, that sample exhibited stretchability exceeding 400% strain. In contrast, GTP-EG2-*co*-C_6F_{13}50 was rigid and fractured below 3% strain. The Young's moduli of GTP-EG2-*co*-C_6F_{13}25 and 50 were 0.47 ± 0.03 GPa and 0.93 ± 0.05 GPa, respectively (mean ± standard error, n = 3).

Surface Properties of GTPs

The surface properties of the GTP−C_6F_{13} and GTP−EG2 homopolymers, as well as their copolymers, were characterized by contact angle measurements. From the contact angles of water, ethylene glycol, and diiodomethane droplets (Figure S11), the dispersive and polar components of the surface energy (γ_d and γ_p, respectively) were calculated using the Owens, Wendt, Rabel and Kaelble method (OWRK method).[38−40] The results are summarized in Figure 6a and Table 3.

The surface energies of the GTP−C_6F_{13} and GTP−EG2 homopolymers were 8.3 ± 2.6 mN m^{-1} and 31.0 ± 9.2 mN m^{-1}, respectively. These values reflect the low surface energy of the fluorocarbon side groups and the hydrophilic nature of the ethylene glycol side groups. The copolymers exhibited surface energies comparable to that of the GTP−C_6F_{13} homopolymer, indicating that their surfaces were predominantly covered with fluorocarbon chains. As shown in Figure 6b, the water contact angle of the GTP-EG2-*co*-C_6F_{13}25 film is comparable to that of the GTP−C_6F_{13} homopolymer film, even though the C_6F_{13} side group is a minor component. Interestingly, the surface energy of GTP-EG2-*co*-C_6F_{13}25 exhibits a markedly smaller polar component (γ_p = 0.8 ± 0.2 mN m^{-1}) than those of the other fluorinated copolymers (γ_p = 2.3−2.7 mN m^{-1}).

To examine the cause of this anomaly, surface roughness was characterized by AFM. Figures 6d and S9 shows AFM images of the GTP films. The results are summarized in Figure 6c and Table 3. The surface roughness of the GTP-EG2 homopolymer and GTP-EG2-*co*-C_6F_{13}25 (R_a < 1 nm) was much smaller than that of the other samples (R_a = 4−15 nm, Table 3). This difference arises from whether the material is fully amorphous. To rationalize the lower polar component of the surface energy observed for the GTP-EG2-*co*-C_6F_{13}25 film, we propose the following hypothesis. A completely flat surface can be uniformly covered with C_6F_{13} side chains, leaving few defect sites that expose the hydrophilic components of the polymer. In contrast, nanometer-scale roughness increases the number of defect sites, thereby exposing more hydrophilic units.

The advancing and receding contact angles (θ_A and θ_R), corresponding to the contact angles measured during the inflation and deflation of a water droplet, respectively, were also characterized (Figure S12).[41,42] Figure 7a shows the advancing contact angle profiles as a function of droplet volume. With the exception of GTP-EG2-*co*-C_6F_{13}25, all GTP surfaces exhibited constant θ_A values, and their baseline widths increased smoothly over the volume range of 5−10 μL (Figure S13a, left). The θ_A values of the GTP-EG2-*co*-C_6F_{13}75, 60, and 50 copolymers were comparable. In contrast, GTP-EG2-*co*-

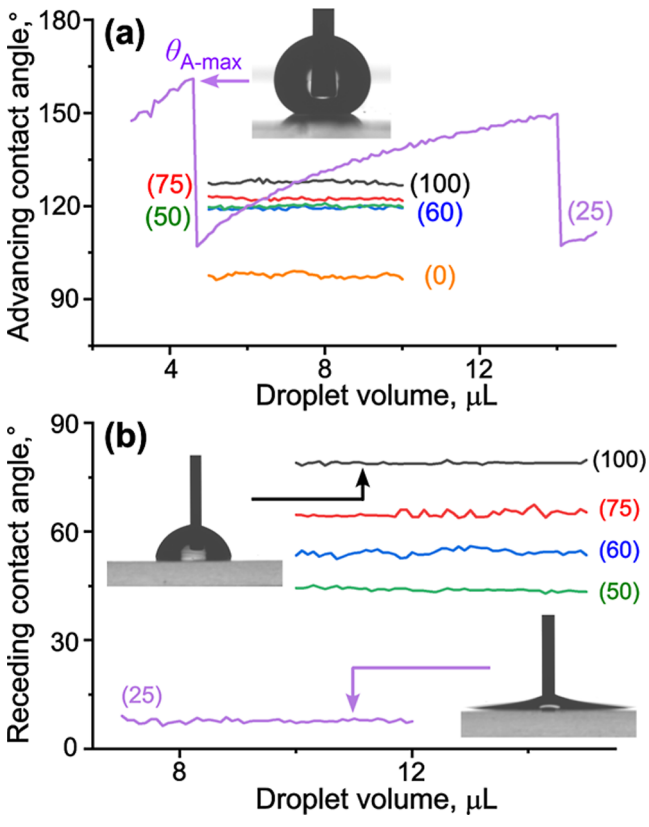

Figure 7. (a) Representative advancing contact angle profiles during the inflation of water droplets. The droplet volume was increased at a rate of 0.1 μL s^{-1}. The number in parentheses indicates the C_6F_{13} content. The inset photograph shows a water droplet exhibiting the maximum advancing contact angle on the GTP-EG2-*co*-C_6F_{13}25 film. (b) Representative receding contact angle profiles during the deflation of water droplets. The droplet volume was decreased at a rate of 0.1 μL s^{-1}. The inset photographs show water droplets on the GTP−C_6F_{13} homopolymer film (top left) and on the GTP-EG2-*co*-C_6F_{13}25 film (bottom right). Droplet volume: 11 μL.

https://doi.org/10.1021/acsapm.5c04519
ACS Appl. Polym. Mater. 2026, 8, 3023−3032

C_6F_{13}25 exhibited a distinctive stick-and-slip behavior (Figure 7a). Because the baseline width remained constant and the θ_A value continued to increase until reaching a critical value, no plateau region appeared in the θ_A profile (Figure S13a, right). Therefore, for this sample, the θ_A value in Table 4 was obtained by averaging the contact angles measured within the 5−10 μL volume range. This stick-and-slip behavior was consistently observed across the entire GTP-EG2-*co*-C_6F_{13}25 film surface. Notably, as shown in the inset photograph of Figure 7a, the maximum advancing contact angle reached 160 ± 2°, surpassing the critical threshold of 150° typically used to define superhydrophobicity.[43]

Table 4. Summary of Advancing and Receding Contact Angles and Contact Angle Hysteresis

sample name	θ_A[a] (°)	$\theta_{A\text{-max}}$[b] (°)	θ_R[c] (°)	$\Delta\theta$[d] (°)
GTP−C_6F_{13}	128 ± 1	−[e]	78 ± 1	50
GTP-EG2-*co*-C_6F_{13}75	120 ± 2	−[e]	65 ± 2	55
GTP-EG2-*co*-C_6F_{13}60	119 ± 2	−[e]	53 ± 1	66
GTP-EG2-*co*-C_6F_{13}50	119 ± 1	−[e]	45 ± 1	74
GTP-EG2-*co*-C_6F_{13}25	(130 ± 3)[f]	160 ± 2	7 ± 1	(>123)[f]
GTP−EG2	93 ± 4	−[e]	(<5)[g]	(>88)[g]

[a]Advancing contact angle of a water droplet. [b]Maximum advancing contact angle in stick-and-slip process. [c]Receding contact angle of a water droplet. Values are presented as mean ± standard deviation (n = 5). [d]Contact angle hysteresis ($\theta_A - \theta_R$). [e]No stick-and-slip behavior was observed. [f]Appropriate advancing contact angle was not obtainable due to stick-and-slip behavior. The data was obtained from the averaged value at the droplet volume from 5 to 10 μL. [g]Appropriate receding contact angle was not obtainable because the contact angle was smaller than 5°.

Figure 7b shows the receding contact angle profiles as a function of droplet volume. Within a certain volume range, the contact line was moving on the surface and the water droplet maintained a constant θ_R value (Figure S13b). Because the θ_R values ranged widely from less than 5° (GTP−EG2) to 80° (GTP−C_6F_{13}), it was not feasible to obtain all measurements within the same volume range. However, since the volume ranges used for calculating the θ_R value of each sample partially overlapped, we considered the data to be mutually comparable. Unlike the advancing contact angle results, the GTP copolymers exhibited distinct, intrinsic θ_R values that decreased as the C_6F_{13} content decreased. Notably, the θ_R value on the GTP-EG2-*co*-C_6F_{13}25 surface was 7 ± 1°, falling below the commonly accepted threshold of 10° used to define superhydrophilicity.[44] It is considered that the superhydrophilicity at the polymer/water interface and superhydrophobicity at the polymer/air interface is responsible for the distinctive stick-and-slip behavior on the surface of GTP-EG2-*co*-C_6F_{13}25.

The contact angle hysteresis ($\Delta\theta$), defined as the difference between the advancing and receding contact angles,[45] is summarized in Table 4. Notably, GTP-EG2-*co*-C_6F_{13}25 exhibited a large $\Delta\theta$ of 123°. If calculated using the maximum advancing contact angle ($\theta_{A\text{-max}}$), $\Delta\theta$ would reach 153°. Large $\Delta\theta$ values are often observed on rough surfaces, a phenomenon known as the rose petal effect, which some researchers reproduce through surface micropatterning.[46−49] For instance, Su et al. reported a $\Delta\theta$ value of 156° for the surface covered with polyelectrolyte-coated submicrometer-scale silica particles,[50] while Mistura et al. reported $\Delta\theta$ values of 100−120° for the surface covered with electrospun polymer nanofibers.[51] Contact angle hysteresis can also be observed on flat surfaces, but a $\Delta\theta$ exceeding 100° is exceptionally rare. For instance, the $\Delta\theta$ values of poly(2-hydroxyethyl methacrylate), poly(acrylic acid), and polyacrylamide derivatives—those are known to exhibit pronounced contact angle hysteresis—range from 20° to 70°.[52,53] Meanwhile, the reported $\Delta\theta$ values for amphiphilic fluorinated copolymers similar to our GTPs range from 60° to 80°.[54,55] The contact angle hysteresis is thought to originate from surface reconstruction driven by molecular interactions between the polymer and water.[45,52,55] The air−polymer interface is considered to be fully covered with C_6F_{13} groups, whereas upon contact with water, the polymer adopts a conformation in which the EG2 side groups are exposed to the polymer/water interface. The amorphous domain is considered to be more advantageous for surface reconstruction than the organized domain, because conformation change is suppressed in the organized domain. Since the fraction of the amorphous domain increases as the C_6F_{13} content decreases, the $\Delta\theta$ value correspondingly increases. The high mobility of the GTP-EG2-*co*-C_6F_{13}25 chains, enabled by a low T_g near room temperature, is also considered to promote surface reconstruction.

CONCLUSION

Using a postpolymerization functionalization approach, high-molecular-weight fluorinated GTPs bearing perfluorohexyl side chains were successfully synthesized. These polymers exhibit excellent thermal, mechanical, and surface properties. Their enhanced thermal stability and tunable mechanical properties are particularly promising for applications in ferroelectric devices. Among the synthesized GTPs, GTP-EG2-*co*-C_6F_{13}25 showed especially distinctive surface behavior. During advancing contact angle measurements, the water droplet exhibited pronounced stick-and-slip motion, with a maximum contact angle exceeding 150°, while the receding contact angle dropped below 10°. This large contact angle hysteresis produces a sticky hydrophobic surface. Such sticky hydrophobic surfaces are attractive for applications requiring precise droplet positioning and strong droplet adhesion, including high-resolution printing, microfluidic manipulation, biosensing, and wearable devices that operate under motion. Notably, GTP-EG2-*co*-C_6F_{13}25 can produce sticky hydrophobic surface without any micropatterning, offering a significant advantage for device fabrication. In the context of global PFAS regulations, perfluorooctanesulfonic acid ($C_8F_{17}SO_3H$) and its related compounds were listed in Annex A of the Stockholm Convention in 2009, which identifies chemicals designated for global elimination. Perfluorohexanesulfonic acid ($C_6F_{13}SO_3H$) and its related compounds were subsequently added to Annex A in 2022. Although the tridecafluoro-1-*n*-octanol used in this study is not included in Annex A, the development of functional fluoropolymers with shorter fluorocarbon chains is an urgent and important challenge. Overall, this study demonstrates that fluorinated GTPs are promising candidates for next-generation functional fluoropolymers. Efforts to develop fluorinated GTPs with even shorter fluorocarbon chains are currently underway.

ASSOCIATED CONTENT

Supporting Information

The Supporting Information is available free of charge at https://pubs.acs.org/doi/10.1021/acsapm.5c04519.

Additional figures: IR spectra, NMR spectra, SEC traces, temperature-dependent XRD profiles, AFM images,

https://doi.org/10.1021/acsapm.5c04519
ACS Appl. Polym. Mater. 2026, 8, 3023−3032

rheological measurements, and contact angle measurements (PDF)

AUTHOR INFORMATION

Corresponding Author

Taichi Ikeda − *Research Center for Macromolecules and Biomaterials, National Institute for Materials Science, Tsukuba, Ibaraki 305-0044, Japan; Biomimetics Center, Tokyo University of Technology, Hachioji, Tokyo 192-0982, Japan;* orcid.org/0000-0001-6650-5798; Email: IKEDA.Taichi@nims.go.jp

Author

Masafumi Yoshio − *Research Center for Macromolecules and Biomaterials, National Institute for Materials Science, Tsukuba, Ibaraki 305-0044, Japan; Graduate School of Chemical Sciences and Engineering, Hokkaido University, Sapporo, Hokkaido 060-8628, Japan; Japan Science and Technology Agency, Precursory Research for Embryonic Science and Technology (PRESTO), Kawaguchi, Saitama 332-0012, Japan;* orcid.org/0000-0002-1442-4352

Complete contact information is available at: https://pubs.acs.org/10.1021/acsapm.5c04519

Author Contributions

T.I.: Conceptualization, synthesis, instrumental analysis, discussion, writing original draft, review and editing, and visualization. M.Y.: Instrumental analysis (XRD), computational modeling, polarized optical microscopy image, discussion, review and revision of the draft.

Notes

The authors declare no competing financial interest.

ACKNOWLEDGMENTS

This work was financially supported by Grant-in-Aids for Scientific Research C, 25K08756 (JSPS). M.Y. also acknowledges financial support from Japan Science and Technology Agency, PRESTO, JPMJPR23QB.

REFERENCES

(1) Chen, Y.; Luo, C.; Hu, F.; Huang, Z.; Yue, K. Recent Advances in Fluorinated Polymers: Synthesis and Diverse Applications. *Sci. China: Chem.* **2023**, *66*, 3347−3359.

(2) Jaye, J. A.; Sletten, E. M. Recent Advances in the Preparation of Semifluorinated Polymers. *Polym. Chem.* **2021**, *12*, 6515−6526.

(3) Hori, H.; Tanaka, H.; Tsuge, T.; Honma, R.; Banerjee, S.; Ameduri, B. Decomposition of Fluoroelastomer: Poly(vinylidene fluoride-*ter*-hexafluoropropylene-*ter*-tetrafluoroethylene) Terpolymer in Subcritical Water. *Eur. Polym. J.* **2017**, *94*, 322−331.

(4) Jing, X.; Yao, L.; Sheng, Y.; Lou, H.; Zhu, H.; Zhang, Q.; Zhu, S. Record-High Adhesion on Low-Surface-Energy Substrates Through Dipole-Dipole Interactions and Frictional Energy Dissipation in Fluorinated Copolymers. *Adv. Funct. Mater.* **2025**, *35*, 2507232.

(5) Ye, Q.; Chen, K.; Zhou, C.; Xu, M.; Chen, M. Light-Driven Organocatalyzed Controlled Radical Copolymerization of (Perfluoroalkyl)ethylenes and Vinyl Esters/Amides. *ACS Macro Lett.* **2024**, *13*, 1640−1646.

(6) Liang, L.; Wen, T.; Xin, J.; Su, C.; Song, K.; Zhao, W.; Liu, H.; Su, G. Fluoropolymer: A Review on Its Emulsion Preparation and Wettability to Solid-Liquid Interface. *Molecules* **2023**, *28*, 905.

(7) Lv, J.; Cheng, Y. Fluoropolymers in Biomedical Applications: State-of-the-Art and Future Perspectives. *Chem. Soc. Rev.* **2021**, *50*, 5435−5467.

(8) Xia, Z.; Hou, X.; Zheng, H.; Li, L.; Feng, Z.; He, J.; Bai, C. Reprocessable Fluoro-Glycidyl Acrylate-Butadiene Rubbers via in Situ Cross-Linker Chain Extension and Hydrophobic Silica: Achieving Enhanced Tensile Strength and Surface Fluorine Enrichment. *ACS Appl. Polym. Mater.* **2025**, *7*, 5077−5088.

(9) Feng, W.; Sun, L.; Jin, Z.; Chen, L.; Liu, Y.; Xu, H.; Wang, C. A Large-Strain and Ultrahigh Energy Density Dielectric Elastomer for Fast Moving Soft Robot. *Nat. Commun.* **2024**, *15*, 4222.

(10) Yi, Z.; Wang, Z.; Li, Y.; Wu, D.; Xue, Y. Improving the Energy Storage Performance of All-Polymer Composites by Blending PVDF and P(VDF-CTFE). *Macromol. Rapid Commun.* **2023**, *44*, 2200728.

(11) Ye, G.; Kuang, Y.; Ma, M.; Peng, X.; Liu, J. Fluorinated Alkyl Chains Terminated Polar Glycol Ether Side Chain for N-Type Organic Thermoelectrics with Enhanced Performance and Air Stability. *Adv. Sci.* **2025**, *12*, 2500571.

(12) Wilson, L. M.; Griffin, A. C. Liquid-Crystalline Behavior in a Series of Fluorocarbon Side-Chain Polyesters. 2. *Macromolecules* **1994**, *27*, 4611−4614.

(13) Xu, W.; Liu, H.; Gao, Y.; Yao, M.; Zhang, B.; Hao, L. Characterization and Comparability Study of a Series of Novel Fluorinated Polyacrylates with a Rigid Cyclohexane Mesogenic Core. *J. Macromol. Sci., Part A: Pure Appl. Chem.* **2024**, *61*, 772−783.

(14) Ibrahim, M.; Li, Y.; Danjaji, H. A.; Wang, Y. Per- and Polyfluoroalkyl Substances and Global Water Resources: An in-Depth Review of Existing Regulatory Frameworks Worldwide. *Int. J. Environ. Sci. Technol.* **2025**, *22*, 8259−8280.

(15) Matsukami, H.; Saito, J.; Wang, Q.; Miyake, Y. Impact of Tightening Environmental Regulations Against Long-Chain Perfluoroalkyl Acids on Composition of Durable Water Repellents Containing Side-Chain Fluorinated Polymers. *Sci. Total Environ.* **2024**, *940*, 173708.

(16) Lohmann, R.; Letcher, R. J. The Universe of Fluorinated Polymers and Polymeric Substances and Potential Environmental Impacts and Concerns. *Curr. Opin. Green Sustainable Chem.* **2023**, *41*, 100795.

(17) Tan, Y.; Wang, F.; Sun, R.-Y.; Wang, M.; Song, F.; Wang, Y.-Z. Crystalline Alkyl Side Chain Enhanced Hydrophobicity-Oleophobicity for Transparent and Durable Low-Surface-Energy Coatings Based on Short Fluorinated Copolymers. *Macromolecules* **2024**, *57*, 5189−5199.

(18) Jiang, J.; Zhang, G.; Wang, Q.; Zhang, Q.; Zhan, X.; Chen, F. Novel Fluorinated Polymers Containing Short Perfluorobutyl Side Chains and Their Super Wetting Performance on Diverse Substrates. *ACS Appl. Mater. Interfaces* **2016**, *8*, 10513−10523.

(19) Shibasaki, Y.; Saitoh, H.; Chiba, K. DSC and X-Ray Studies on Side-Chain Crystallization of Comb-Like Polymers: Fluorinated *N*-Alkyl Acrylate and Methacrylate Polymers. *J. Therm. Anal.* **1997**, *49*, 115−121.

(20) Honda, K.; Morita, M.; Otsuka, H.; Takahara, A. Molecular Aggregation Structure and Surface Properties of Poly(fluoroalkyl acrylate) Thin Films. *Macromolecules* **2005**, *38*, 5699−5705.

(21) Corpart, J.-M.; Girault, S.; Juhué, D. Structure and Surface Properties of Liquid Crystalline Fluoroalkyl Polyacrylates: Role of the Spacer. *Langmuir* **2001**, *17*, 7237−7244.

(22) Wang, Q.; Zhang, Q.; Zhan, X.; Chen, F. Structure and Surface Properties of Polyacrylates with Short Fluorocarbon Side Chain: Role of the Main Chain and Spacer Group. *J. Polym. Sci., Part A: Polym. Chem.* **2010**, *48*, 2584−2593.

(23) Yamaguchi, H.; Kikuchi, M.; Kobayashi, M.; Ogawa, H.; Masunaga, H.; Sakata, O.; Takahara, A. Influence of Molecular Weight Dispersity of Poly{2-(perfluorooctyl)ethyl acrylate} Brushes on Their Molecular Aggregation States and Wetting Behavior. *Macromolecules* **2012**, *45*, 1509−1516.

(24) Han, D. J.; Kim, S.; Heo, H. J.; Park, I. J.; Kang, H. S.; Lee, S. G.; Lee, J.-C.; Sohn, E.-H. Access to Fluorinated Polymer Surfaces with Outstanding Mechanical Property, High Optical Transparency, and Low Surface Energy via Nonafluoro-*tert*-Butyl Group Introduction. *ACS Appl. Polym. Mater.* **2020**, *2*, 3957−3965.

(25) Chung, J.-S.; Kim, B. G.; Sohn, E.-H.; Lee, J.-C. Molecular Structure and Surface Properties of Comb-Like Fluorinated Poly-(oxyethylene)s Having Different Content of Fluoroalkyl Side Group. *Macromolecules* **2010**, *43*, 10481−10489.
(26) Liu, D.; Zheng, Y.; Steffen, W.; Wagner, M.; Butt, H.-J.; Ikeda, T. Glycidyl 4-Functionalized-1,2,3-Triazole Polymers. *Macromol. Chem. Phys.* **2013**, *214*, 56−61.
(27) Ikeda, T. Glycidyl Triazolyl Polymers: Poly(ethylene glycol) Derivatives Functionalized by Azide−Alkyne Cycloaddition Reaction. *Macromol. Rapid Commun.* **2018**, *39*, 1700825.
(28) Ikeda, T. Poly(ionic liquid)s Based on Copolymers of Poly(ethylene oxide) and Cationic Glycidyl Triazolyl Polymers with Tribranched Side Chains. *ACS Macro Lett.* **2021**, *10*, 831−836.
(29) Ikeda, T. Copper-Free Synthesis of Cationic Glycidyl Triazolyl Polymers. *Macromol. Rapid Commun.* **2024**, *45*, 2400416.
(30) Ikeda, T.; Hosoda, N. Facile, Efficient, and Safe Copper-Free Synthesis of Glycidyl Triazolyl Polymers. *J. Polym. Sci.* **2025**, *63*, 2568−2578.
(31) Touidjine, S.; Boulkadid, M. K.; Trache, D.; Akbi, H.; Guettiche, D.; Belkhiri, S.; Nourine, M. Review on Energetic Copolymer Binders for Propulsion Applications: Synthesis and Properties. *J. Polym. Sci.* **2023**, *61*, 2254−2275.
(32) Obadia, M. M.; Jourdain, A.; Serghei, A.; Ikeda, T.; Drockenmuller, E. Cationic and Dicationic 1,2,3-Triazolium-Based Poly(ethylene glycol ionic liquid)s. *Polym. Chem.* **2017**, *8*, 910−917.
(33) Lebeau, A.; Abrioux, C.; Bénimèlis, D.; Benfodda, Z.; Meffre, P. Synthesis of 1,4-Disubstituted 1,2,3-Triazole Derivatives Using Click Chemistry and Their Src Kinase Activities. *Med. Chem.* **2016**, *13*, 40−48.
(34) Ikeda, T. Copper-Free Synthesis of Glycidyl Triazolyl Polymers. *Macromol. Chem. Phys.* **2018**, *219*, 1800147.
(35) Koda, Y.; Terashima, T.; Sawamoto, M. Multimode Self-Folding Polymers via Reversible and Thermoresponsive Self-Assembly of Amphiphilic/Fluorous Random Copolymers. *Macromolecules* **2016**, *49*, 4534−4543.
(36) Liu, Y.; Higaki, Y.; Mukai, M.; Ohta, N.; Kabe, T.; Takahara, A. Smectic Ordered Structure and Water Repellency of a Poly-(fluoroalkyl acrylate) with a Carbamate Linker. *Polym. J.* **2019**, *51*, 189−198.
(37) Wilson, L. M.; Griffin, A. C. Liquid Crystalline Fluorocarbon Side-Chain Polyesters. *Macromolecules* **1994**, *27*, 1928−1931.
(38) Owens, D. K.; Wendt, R. C. Estimation of the Surface Free Energy of Polymers. *J. Appl. Polym. Sci.* **1969**, *13*, 1741−1747.
(39) Parreidt, T. S.; Schmid, M.; Hauser, C. Validation of a Novel Technique and Evaluation of the Surface Free Energy of Food. *Foods* **2017**, *6*, 31.
(40) Le Brouster, R.; Giboz, J.; Nourdine, A.; Tenchine, L.; Martin, V.; Mele, P. Prediction of Surface Segregation of Fluorinated Additives from Measurement of Wettability Properties of Polymer-Based Blends. *Langmuir* **2024**, *40*, 18305−18313.
(41) Butt, H.-J.; Liu, J.; Koynov, K.; Straub, B.; Hinduja, C.; Roismann, I.; Berger, R.; Li, X.; Vollmer, D.; Steffen, W.; Kappl, M. Contact Angle Hysteresis. *Curr. Opin. Colloid Interface Sci.* **2022**, *59*, 101574.
(42) Huhtamäki, T.; Tian, X.; Korhonen, J. T.; Ras, R. H. A. Surface-Wetting Characterization Using Contact-Angle Measurements. *Nat. Protoc.* **2018**, *13*, 1521−1538.
(43) Ghazala, R.; Askari, M. A.; Guo, S.; Chen, Z.; Xu, B.; Wang, X. Nature-Inspired Interface Fluid Behaviors, Superhydrophobic Material Design, and Droplet Dynamics: A Systematic Review. *Nanoscale* **2026**, *18*, 603−639.
(44) Liu, Z.; Liu, F. Recent Progress on the Healing Mechanisms of Self-Healing Superhydrophilic Surfaces. *Coatings* **2025**, *15*, 1006.
(45) Zhang, H.; Zhang, H.; Wang, F.; Nestler, B. Exploration of Contact Angle Hysteresis Mechanisms: From Microscopic to Macroscopic. *J. Chem. Phys.* **2024**, *161*, 194705.
(46) Feng, L.; Zhang, Y.; Xi, J.; Zhu, Y.; Wang, N.; Xia, F.; Jiang, L. Petal Effect: A Superhydrophobic State with High Adhesive Force. *Langmuir* **2008**, *24*, 4114−4119.
(47) Chang, F.-M.; Hong, S.-J.; Sheng, Y.-J.; Tsao, H.-K. High Contact Angle Hysteresis of Superhydrophobic Surfaces: Hydrophobic Defects. *Appl. Phys. Lett.* **2009**, *95*, 064102.
(48) Reyssat, M.; Quéré, D. Contact Angle Hysteresis Generated by Strong Dilute Defects. *J. Phys. Chem. B* **2009**, *113*, 3906−3909.
(49) Zhang, Y.; Xue, Y.; Li, M.; Zhang, Y. 3D Printing for Super-Wetting Surfaces. *Adv. Mater. Technol.* **2025**, *10*, No. e01049.
(50) Wang, L.; Wei, J.; Su, Z. Fabrication of Surfaces with Extremely High Contact Angle Hysteresis from Polyelectrolyte Multilayer. *Langmuir* **2011**, *27*, 15299−15304.
(51) Varagnolo, S.; Raccanello, F.; Pierno, M.; Mistura, G.; Moffa, M.; Persano, L.; Pisignano, D. Highly Sticky Surfaces Made by Electrospun Polymer Nanofibers. *RSC Adv.* **2017**, *7*, 5836−5842.
(52) Morra, M.; Occhiello, E.; Garbassi, F. On the Wettability of Poly(2-hydroxyethylmethacrylate). *J. Colloid Interface Sci.* **1992**, *149*, 84−91.
(53) Extrand, C. W. Water Contact Angles and Hysteresis of Polyamide Surfaces. *J. Colloid Interface Sci.* **2002**, *248*, 136−142.
(54) Takahashi, S.; Kasemura, T.; Asano, K. Surface Molecular Mobility for Copolymers Having Perfluorooctyl and/or Polyether Side Chains via Dynamic Contact Angle. *Polymer* **1997**, *38*, 2107−2111.
(55) Tokuda, K.; Kawasaki, M.; Kotera, M.; Nishino, T. Highly Water Repellent but Highly Adhesive Surface with Segregation of Poly(ethylene oxide) Side Chains. *Langmuir* **2015**, *31*, 209−214.

https://doi.org/10.1021/acsapm.5c04519
ACS Appl. Polym. Mater. 2026, 8, 3023−3032